Available online at www.sciencedirect.com

SCIENCE DIRECT®

Journal of Computational Physics 208 (2005) 1–33

JOURNAL OF
COMPUTATIONAL
PHYSICS

www.elsevier.com/locate/jcp

A second-order-accurate monotone implicit fluctuation splitting scheme for unsteady problems

P. De Palma *, G. Pascazio, G. Rossiello, M. Napolitano

Dipartimento di Ingegneria Meccanica e Gestionale, Centro di Eccellenza in Meccanica Computazionale, Politecnico di Bari, Via Re David 200, 70125 Bari, Italy

Received 27 October 2003; received in revised form 23 November 2004; accepted 23 November 2004
Available online 23 December 2004

Abstract

This paper provides an implicit fluctuation splitting scheme which achieves second-order accuracy in both space and time, while guaranteeing monotone solutions. The method is based on a dual-time-stepping approach which allows to separate the spatial and temporal discretizations. A novel distribution scheme of the unsteady-fluctuation term, coupled with a new limiting procedure for hampering spurious extrema, are the key-ingredients of the remarkable accuracy of the new method, which is applied with success to both scalar advection problems and unsteady inviscid flows in two space dimensions.

Keywords: Residual distribution method; Unsteady hyperbolic equations; Consistent mass matrix; Dual-time-stepping technique; Monotone solutions

1. Introduction

During the last decade, a significant research effort has been devoted to the improvement of upwind schemes for the solution of the Euler and Navier–Stokes equations for compressible flows. Two methods emerged as promising alternatives to standard finite volume flux difference splitting or flux vector splitting schemes [1,2], namely, the discontinuous Galerkin (DG) method [3] and the residual distribution or fluctuation splitting (FS) approach [4,5]. They share a very important property, the compactness of the scheme, which renders them suitable for modern parallel computers. The DG method is a generalization of the

---

* Corresponding author. Tel.: +39 80 596 3226; fax: +39 80 596 3411.
E-mail addresses: depalma@poliba.it (P. De Palma), pascazio@poliba.it (G. Pascazio), g.rossiello@poliba.it (G. Rossiello), napolita@poliba.it (M. Napolitano).

0021-9991/$ - see front matter © 2004 Elsevier Inc. All rights reserved.
doi:10.1016/j.jcp.2004.11.023

classical Galerkin finite element method, embedding the solution of the Riemann problem as a model for propagation phenomena by using a discontinuous solution reconstruction. The FS approach is based on a continuous reconstruction of the solution, the residual, namely, the flux balance over each computational cell, being distributed among the vertices of the cell with an upwind bias. Due to such a distribution step, which can properly mimic the convection of signals regardless of the grid orientation, FS schemes can be considered truly multidimensional. In the present paper, the FS approach is considered. After the pioneering work of Roe, Deconinck and their associates [4,6–9], the new methodology was further developed and applied to solve a wide range of compressible steady flows [10–13]. More recently, following the general trend of CFD to attack more realistic unsteady flow problems, several attempts at generalizing FS schemes to the unsteady-flow equations have been proposed [14–19]. Such a goal turned out to be all but straightforward, so that different approaches were to be pursued. The simplest choice would be employing the method of lines which, unfortunately, cannot be successful. In fact, recasting the problem into the variational formulation, it turns out that, in general, second-order accuracy in space and time cannot be achieved without employing a suitable consistent mass matrix which, on the other hand, renders the scheme implicit. Actually, the only way to achieve second-order accuracy using an explicit FS scheme appears to be the Lax–Wendroff scheme, equivalent to a Taylor–Galerkin discretization with a suitable mass-lumping, which renders the scheme explicit without affecting its order of accuracy [16]. Such a scheme, being linear and second-order-accurate, is not positive. First attempts to design monotone FS schemes for unsteady problems were based on the use of the Lax–Wendroff scheme in conjunction with a flux-corrected transport (FCT) strategy [20], which allows to recover positivity by modifying the signals sent by each triangle to its nodes [16,21]. Unfortunately, such schemes have been seen to provide unsatisfactory phase errors due to the use of the Lax–Wendroff scheme. On the other hand, in [15] a consistent mass matrix formulation was considered, again employing an FCT procedure applied to the triangle signals, together with the Crank–Nicolson scheme. Such an approach lacks robustness and does not allow to reduce the unsteady residual to machine zero by any iterative procedure. More recently, Csík et al. [17] and Abgrall and Mezine [19] have proposed two different approaches in the framework of the more general space–time residual distribution schemes, both based on continuous space–time elements. The first authors employ prismatic elements, whereas the second ones use tetrahedra in the space–time domain. Both methods are implicit and may employ two layers of cells in the temporal direction in order to achieve unconditional stability. In this way, nonlinear FS schemes can be extended to space–time elements damping spurious oscillations. Nevertheless, two drawbacks remain: (i) second-order-accurate nonlinear FS schemes cannot achieve machine zero when an iterative procedure, such as the Newton method, is employed, as correctly acknowledged in [19]; (ii) the use of nonlinear positive FS schemes, such as the PSI [4] or the N-modified [19] ones, in low-gradient regions appears to be undesirable since they are clearly more dissipative than linearity preserving linear FS schemes, such as the LDA one [4]. The aim of this paper is to provide a contribution towards developing a monotone FS scheme for unsteady flow problems which achieves second-order accuracy in both space and time. An implicit scheme is proposed which addresses the two issues above while providing improved accuracy with respect to the scheme of [16,21]. The scheme, which employs a dual-time-stepping procedure, is based on two main contributions: (i) a general formulation of the consistent mass matrix; (ii) a new limiting procedure to achieve monotone solutions. Such a procedure is similar to the FCT one, insofar as it allows to control the solution, locally, in order to avoid the creation of spurious extrema, and, most importantly, it is employed at each node, after collecting the residual from the neighbouring elements, instead of at each triangle. In this way, the limiting procedure does not prevent reducing the residual to machine-zero, a feature which is fundamental for the use of any iterative solver.

The paper proceeds as follows. The basic FS schemes are briefly reviewed and the FCT strategy, which allowed for the first time to achieve second-order-accurate monotone unsteady-flow solutions, is explained in some detail. Particular attention is devoted to the key new features of the proposed approach, namely, the determination of the generalized mass matrix and the application of the limiting procedure to each node rather than to each triangle. The method is described for the simple case of the scalar advection equation and is then extended to the Euler system. The accuracy of the scheme is verified numerically for both the scalar equation and the Euler system employing two problems having known exact solutions. Finally, the method is tested versus two very severe unsteady flows with shocks.

2. Scalar advection equation

In this section multidimensional discretization methods, which are second-order-accurate in space and time, are presented with reference to the two-dimensional scalar advection equation. After a brief review of the FS approach and of the four basic FS schemes of interest, the explicit scheme of [16,21] is recalled, which is based on the combination of two FS schemes with the FCT strategy to control local extrema. Such an approach represents a well-established technique to design residual distribution schemes for the unsteady scalar advection equation. Then, a new implicit FS scheme is proposed together with a novel limiting procedure designed to suppress spurious extrema.

2.1. The FS approach

Consider the two-dimensional linear advection equation for the scalar variable u,

$$\frac{\partial u}{\partial t} = -\left(a\frac{\partial u}{\partial x} + b\frac{\partial u}{\partial y}\right). \tag{1}$$

The computational domain is discretized by triangular elements. If the variable u is assumed to vary linearly over each triangle, the discrete fluctuation, namely, the flux balance over the cell, can be evaluated exactly as:

$$\phi_T = -\sum_{j=1}^{3} k_j u_j, \quad k_j = \frac{1}{2}\boldsymbol{\lambda}\cdot\boldsymbol{n}_j l_j, \tag{2}$$

$\boldsymbol{\lambda}$, $\boldsymbol{n}_j$ and l_j being the advection velocity, the inward unit normal to the edge opposing node j and its length, respectively. Fluctuation splitting schemes are obtained by two main steps: (i) the fluctuation is distributed among the nodes j of each triangle; (ii) the solution at each node i of the computational domain is obtained by summing up all nodal contributions (arising from the set of triangles sharing node i, Δ_i) as:

$$u_i^{n+1} = u_i^n + \frac{\Delta t}{|S_i|}\sum_{T\in\Delta_i}\beta_{T,i}\phi_T = u_i^n + \frac{\Delta t}{|S_i|}\sum_{T\in\Delta_i}\phi_{T,i}, \tag{3}$$

where S_i is the dual cell associated with node i, $|S_i|$ is its area, and Δt is the time step. Several FS schemes have been proposed in the literature, the final goal being a monotone and second-order-accurate scheme, an impossible task for any linear scheme [4]. Most of such schemes are of the (multidimensional) upwind type: with reference to Fig. 1, linearly interpolated values of u at the inflow and outflow points of the cell can be evaluated as

$$u_{\text{in}} = \frac{\sum_{j=1}^{3}k_j^- u_j}{\sum_{j=1}^{3}k_j^-}, \quad u_{\text{out}} = \frac{\sum_{j=1}^{3}k_j^+ u_j}{\sum_{j=1}^{3}k_j^+}, \tag{4}$$

where $k_j^+ = \max(0, k_j)$, $k_j^- = \min(0, k_j)$; then, the fluctuation, ϕ_T, can be written in compact form as [22]

$$\phi_T = -\sum_{j=1}^{3}k_j u_j = -\sum_{j=1}^{3}k_j^+(u_{\text{out}} - u_{\text{in}}). \tag{5}$$

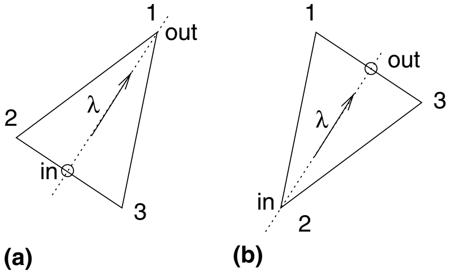

Fig. 1. Definition of inflow and outflow points: (a) one target case; (b) two target case.

Eq. (5) shows that the fluctuation is zero when u takes the same values at both the inflow and outflow points, namely, when it is constant along streamlines. Upwind schemes are obtained by assigning to each downstream node j, $k_j \geqslant 0$, a fraction $\beta_{T,j}$ of the cell-fluctuation ($\sum_{j=1}^{3}\beta_{T,j} = 1\ \forall T$, for conservation). In the trivial configuration 1(a), the entire fluctuation is assigned to the only downstream node and the resulting FS scheme is both positive and second-order-accurate. For the non-trivial configuration 1(b), different choices of the distribution coefficients $\beta_{T,j}$ characterize the different schemes.

For the present study of unsteady inviscid flows, the following FS schemes are of interest:

(1) The N scheme, which is the optimal first-order-accurate upwind scheme [4]:

$$\phi_j^{\mathrm{N}} = -k_j^{+}(u_j - u_{\mathrm{in}}). \tag{6}$$

(2) The non-upwind FS Lax–Wendroff (FS-LW) scheme [22]:

$$\phi_j^{\mathrm{LW}} = \left(\frac{1}{3} + \frac{\Delta t}{2|T|}k_j\right)\phi_T = \beta_{T,j}^{\mathrm{LW}}\phi_T, \tag{7}$$

where $|T|$ is the area of triangle T. Such a scheme is the unique explicit FS scheme with second-order accuracy in space and time (see, e.g., [16,22]).

(3) The second-order-accurate non-monotone upwind control volume (UCV) scheme [22]:

$$\phi_j^{\mathrm{UCV}} = \left(\frac{1}{3} + \frac{2}{3}\frac{k_j}{\sum_{i=1}^{3}|k_i|}\right)\phi_T = \beta_{T,j}^{\mathrm{UCV}}\phi_T. \tag{8}$$

(4) The second-order-accurate non-monotone low diffusion A (LDA) scheme [22]:

$$\phi_j^{\mathrm{LDA}} = \left(\frac{k_j^{+}}{\sum_{i=1}^{3}k_i^{+}}\right)\phi_T = \beta_{T,j}^{\mathrm{LDA}}\phi_T. \tag{9}$$

2.2. The FCT explicit scheme

A first approach [16,21] which has been pursued to design a monotone FS scheme, which is second-order-accurate in both space and time, is based on the FCT strategy [20], employing the N scheme as the lower-order (lo) scheme and the FS-LW scheme as the higher-order (ho) one. Such a scheme will be referred to as FS-FCT scheme. The entire procedure is described here in detail.

(1) For each node j of each element T:
   (a) compute the lower-order contribution (ϕ_j^{N}), using the N scheme;
   (b) compute the higher-order contribution (ϕ_j^{LW}), using the FS-LW scheme;
   (c) compute the anti-diffusive correction (ac_j):

$$ac_j = \frac{\Delta t}{|S_j|}(\phi_j^{\mathrm{LW}} - \phi_j^{\mathrm{N}}).$$

(2) For each node i of the domain compute the lower-order solution:

$$u_i^{\mathrm{lo}} = u_i^n + \frac{\Delta t}{|S_i|}\sum_{T\in\Delta_i}\phi_{T,i}^{\mathrm{N}}.$$

(3) For each element evaluate the limiter σ_T for the ac_j terms which avoids the creation of spurious extrema as described later.

(4) For each node i of the domain compute the final solution at the new time level $n + 1$ as

$$u_i^{n+1} = u_i^{\mathrm{lo}} + \sum_{T\in\Delta_i}\sigma_T ac_i^T.$$

The limiter σ_T is evaluated as follows.

(1) For each node i of the domain compute the quantities:

$$u_i^{\pm} = \begin{cases}\max\\ \min\end{cases}(u_i^{\mathrm{lo}}, u_i^n).$$

(2) For each element T, compute the quantities:

$$u_T^{\pm} = \begin{cases}\max\\ \min\end{cases} u_j^{\pm} \quad \forall j \in T.$$

(3) For each node i compute the quantities:

$$\bar{u}_i^{\pm} = \begin{cases}\max\\ \min\end{cases} u_T^{\pm} \quad \forall T \in \Delta_i,$$

which represent the extreme values that the solution may assume at node i, i.e., $\bar{u}_i^- \leqslant u_i^{n+1} \leqslant \bar{u}_i^+$.

(4) For each node i compute the quantities:

$$p_i^{\pm} = \sum_{T\in\Delta_i}\begin{matrix}\max\\ \min\end{matrix}(0, ac_i^T),$$

$$q_i^{\pm} = \bar{u}_i^{\pm} - u_i^{\mathrm{lo}},$$

$$w_i^{\pm} = \begin{cases}\min(1, q_i^{\pm}/p_i^{\pm}) & \text{if } p_i^+ > 0,\ p_i^- < 0,\\ 0 & \text{if } p_i^{\pm} = 0;\end{cases}$$

$w_i^{\pm}$ are the limiting factors for the antidiffusive correction, ac_i^T, which guarantee that the solution at the new time level satisfies the lower and upper bounds, $\bar{u}_i^-$ and $\bar{u}_i^+$, determined at step (3).

(5) For each node j of each element T, compute

$$\sigma_j^T = \begin{cases} w_j^+ & \text{if } ac_j^T \geqslant 0, \\ w_j^- & \text{if } ac_j^T < 0. \end{cases}$$

(6) Finally,

$$\sigma_T = \min \sigma_j^T \quad \forall j \in T.$$

Notice that the limiter is the same for all nodes of each triangle, for conservation.

As shown in the result section, the main drawback of such a procedure is its unsatisfactory lagging phase error due to the use of the FS-LW scheme. In order to overcome such a difficulty, different strategies can be pursued, such as those based upon space–time residual distribution methods [17,19]. In the present paper, second-order accuracy for the unsteady problem is achieved by embedding a consistent mass-matrix formulation and a second-order-accurate distribution scheme within a dual-time-stepping procedure using a three-point backward implicit time integration scheme.

2.3. The proposed implicit scheme

The proposed scheme is based on a second-order-accurate three-level discretization of the time derivative and a dual-time-stepping technique [23]. Each step in the fictitious time can be written as:

$$u_i^{n+1,k+1} = u_i^{n+1,k} - \frac{\Delta\tau}{|S_i|} \sum_{T\in\Delta_i} (\alpha_{T,i}\phi_T^t - \beta_{T,i}\phi_T)^{n+1,k}, \tag{10}$$

where

$$\phi_T^t = \int_T \frac{\partial u}{\partial t}\,\mathrm{d}S = \frac{|T|}{3}\sum_{i=1}^{3}\left(\frac{\partial u}{\partial t}\right)_i, \quad \left(\frac{\partial u}{\partial t}\right)_i = \frac{3u_i^{n+1} - 4u_i^n + u_i^{n-1}}{2\Delta t}.$$

Concerning the discretization of the critical unsteady term, ϕ_T^t, the distribution coefficients $\alpha_{T,i}$ read:

$$\alpha_{T,i} = \frac{1}{\phi_T^t}\int_{A_i} \frac{\partial u}{\partial t}\,\mathrm{d}S, \quad A_i = S_i \cap T, \ \ \mathrm{area}(A_i) = |A_i|. \tag{11}$$

The integral in the previous equation is to be extended to the portion, A_i, of each triangle $T \in \Delta_i$ (see Fig. 2), which contributes to the dual cell $S_i = \cup_{T\in\Delta_i} A_i$, in order to be consistent with the spatial discretization, thus guaranteeing second-order accuracy in space and time. Such a fraction of the area is uniquely defined by the steady distribution coefficients, $|A_i| = \beta_{T,i}|T|$, being

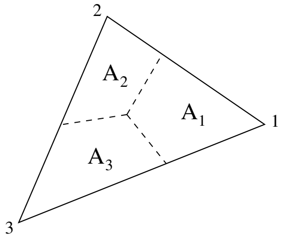

Fig. 2. Triangle partition.

$$-\int_{A_i} \boldsymbol{\lambda} \cdot \nabla u \, \mathrm{d}S = \frac{\phi_T}{|T|} |A_i| = \phi_{T,i} = \beta_{T,i} \phi_T. \tag{12}$$

Combining the temporal and spatial contributions, one has:

$$\alpha_{T,i} \phi_T^t - \beta_{T,i} \phi_T = \int_{A_i} \left(\frac{\partial u}{\partial t} + \boldsymbol{\lambda} \cdot \nabla u \right) \mathrm{d}S. \tag{13}$$

The integral in Eq. (11) is evaluated analytically, the time derivative varying linearly over the triangle, according to the following procedure:

$$\int_{A_i} \frac{\partial u}{\partial t} \, \mathrm{d}S = \hat{u}_{,t}^{A_i} |A_i|, \tag{14}$$

where $\hat{u}_{,t}^{A_i}$ is the average value of the time derivative over the portion A_i. Such a value can be written as:

$$\hat{u}_{,t}^{A_i} = \sum_{j=1}^{3} \gamma_{i,j} (u_{,t})_j, \tag{15}$$

with

$$\sum_{j=1}^{3} \gamma_{i,j} = 1. \tag{16}$$

Employing Eqs. (14) and (15), one has:

$$\int_{A_i} \frac{\partial u}{\partial t} \, \mathrm{d}S = |T| \sum_{j=1}^{3} \beta_{T,i} \gamma_{i,j} (u_{,t})_j = \sum_{j=1}^{3} m_{i,j} (u_{,t})_j, \tag{17}$$

where the condition $|A_i| = \beta_{T,i}|T|$ has been used and $m_{i,j} = |T|\beta_{T,i}\, \gamma_{i,j}$ is the mass matrix. Since

$$\int_{T} \frac{\partial u}{\partial t} \, \mathrm{d}S = \frac{|T|}{3} \sum_{j=1}^{3} (u_{,t})_j \tag{18}$$

and

$$\int_{T} \frac{\partial u}{\partial t} \, \mathrm{d}S = \sum_{i=1}^{3} \int_{A_i} \frac{\partial u}{\partial t} \, \mathrm{d}S = |T| \sum_{i=1}^{3} \sum_{j=1}^{3} \beta_{T,i} \gamma_{i,j} (u_{,t})_j, \tag{19}$$

it follows that

$$\sum_{i=1}^{3} \beta_{T,i} \gamma_{i,j} = \frac{1}{3}. \tag{20}$$

Eqs. (16) and (20) are the six conditions to be satisfied by the nine unknowns $\gamma_{i,j}$ to achieve second-order accuracy. One possible strategy to close the problem, which has been proposed in [18], consists in dividing each triangle into three areas, $|A_i| = |T|/3$, employing the medians. Therefore, integrating exactly Eq. (14) one obtains:

$$\gamma_{i,i} = \frac{22}{36} \quad \text{and} \quad \gamma_{i,j} = \frac{7}{36}, \tag{21}$$

and second-order accuracy is obtained employing $\beta_{T,i} = 1/3$. Such a centred scheme is used in [18], where artificial dissipation is added for stability.

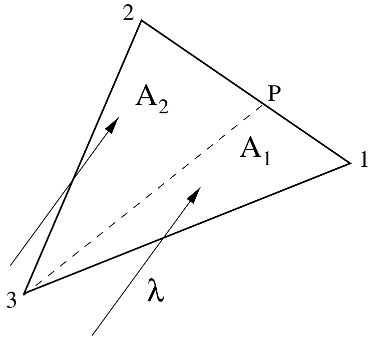

Fig. 3. Two target configuration.

In the present paper a different approach is taken. The conditions needed to close the problem are determined so as to guarantee that in the *two-target case* (shown in Fig. 1(b)) the unsteady term is distributed only between the downstream nodes according to Eq. (11). Let us consider the triangle in Fig. 3 in which the spatial fluctuation is distributed between nodes 1 and 2. Such a triangle is divided into two areas, $|A_1| = \beta_{T,1}|T|$ and $|A_2| = \beta_{T,2}|T|$. The average value of $u_{,t}$ over A_1 is given as

$$\hat{u}_{,t}^{A_1} = \frac{(u_{,t})_1 + (u_{,t})_P + (u_{,t})_3}{3}, \tag{22}$$

where $(u_{,t})_P$ is the value at point P on the outflow edge 1–2:

$$(u_{,t})_P = \frac{|A_2|(u_{,t})_1 + |A_1|(u_{,t})_2}{|T|} = \beta_{T,2}(u_{,t})_1 + \beta_{T,1}(u_{,t})_2. \tag{23}$$

Substituting Eq. (23) in Eq. (22), one has:

$$\hat{u}_{,t}^{A_1} = \frac{2-\beta_{T,1}}{3}(u_{,t})_1 + \frac{1-\beta_{T,2}}{3}(u_{,t})_2 + \frac{1}{3}(u_{,t})_3. \tag{24}$$

Generalizing the coefficients of the three terms in Eq. (24), the coefficients in Eq. (15) are seen to be:

$$\gamma_{i,i} = \frac{2-\beta_{T,i}}{3}, \qquad \gamma_{i,j} = \frac{1-\beta_{T,j}}{3}, \quad j \neq i. \tag{25}$$

The general form of the mass matrix for the proposed scheme reads:

$$m_{i,j} = \frac{|T|}{3}\begin{bmatrix} \beta_{T,1}(2-\beta_{T,1}) & \beta_{T,1}(1-\beta_{T,2}) & \beta_{T,1}(1-\beta_{T,3}) \\ \beta_{T,2}(1-\beta_{T,1}) & \beta_{T,2}(2-\beta_{T,2}) & \beta_{T,2}(1-\beta_{T,3}) \\ \beta_{T,3}(1-\beta_{T,1}) & \beta_{T,3}(1-\beta_{T,2}) & \beta_{T,3}(2-\beta_{T,3}) \end{bmatrix}. \tag{26}$$

Two additional schemes can be obtained straightforwardly assuming either

$$\alpha_{T,i} = \beta_{T,i}, \tag{27}$$

or

$$\alpha_{T,i} = 1/3. \tag{28}$$

Combining Eqs. (11) and (17) one has:

$$|T|\beta_{T,i}\sum_{j=1}^{3}\gamma_{i,j}(u_{,t})_j = \alpha_{T,i}\phi_T^t. \tag{29}$$

Eq. (29): (i) combined with condition (27) leads to $\gamma_{i,j} = 1/3$, providing a second-order-accurate scheme; (ii) combined with condition (28) gives $\gamma_{i,j} = 1/(9\ \beta_{T,i})$, which violates Eq. (20) when $\beta_{T,i} = 0$ so that the scheme is only first-order-accurate. The mass matrices corresponding to the two schemes defined by Eqs. (27) and (28) are given as:

$$m_{i,j} = \frac{|T|}{3}\begin{bmatrix} \beta_{T,1} & \beta_{T,1} & \beta_{T,1} \\ \beta_{T,2} & \beta_{T,2} & \beta_{T,2} \\ \beta_{T,3} & \beta_{T,3} & \beta_{T,3} \end{bmatrix}, \tag{30}$$

$$m_{i,j} = \frac{|T|}{3}\begin{bmatrix} \frac{1}{3} & \frac{1}{3} & \frac{1}{3} \\ \frac{1}{3} & \frac{1}{3} & \frac{1}{3} \\ \frac{1}{3} & \frac{1}{3} & \frac{1}{3} \end{bmatrix}. \tag{31}$$

For comparison, the consistent mass matrix derived in [14] is also reported here:

$$m_{i,j} = \frac{|T|}{3}\begin{bmatrix} \beta_{T,1}+\frac{1}{6} & \beta_{T,1}-\frac{1}{12} & \beta_{T,1}-\frac{1}{12} \\ \beta_{T,2}-\frac{1}{12} & \beta_{T,2}+\frac{1}{6} & \beta_{T,2}-\frac{1}{12} \\ \beta_{T,3}-\frac{1}{12} & \beta_{T,3}-\frac{1}{12} & \beta_{T,3}+\frac{1}{6} \end{bmatrix}. \tag{32}$$

Such a matrix has been obtained in a finite element framework by employing linear shape functions, N_i, and a test function, ω_i, defined as $\omega_i = N_i + \beta_i - \frac{1}{3}$.

In the present paper, the UCV space distribution coefficients have been used and the schemes obtained employing Eqs. (25), (27) and (28) will be referred to as MM-CU (mass matrix-consistent upwind), MM-SU (simple upwind), and MM-C (centred), respectively, whereas the scheme corresponding to matrix (32) will be denoted as MM-PG (Petrov–Galerkin). Needless to say, the MM-C scheme is anticipated to be markedly inferior to the other ones.

3. The proposed limiting procedure

The FCT strategy described in Section 2.2, although devised for explicit schemes, could be extended in principle to implicit ones, by employing a dual-time-stepping technique. Unfortunately, due to the nonlinearity of the limiting procedure, the residual drop in the pseudo-time is limited to two/three orders of magnitude. Therefore, a new limiting procedure is devised which overcomes such a difficulty by using the nodal values of the lower- and higher-order solutions rather than the triangle contributions. The entire procedure is described here in detail.

(1) For each node i of the domain, compute the lower-order, u_i^{lo}, and higher-order, u_i^{ho}, solutions, and the quantities:

$$u_i^{\pm} = \begin{cases} \max \\ \min \end{cases} (u_i^{\mathrm{lo}}, u_i^{n}).$$

(2) For each element T, compute the quantities:

$$u_T^{\pm} = \begin{cases} \max \\ \min \end{cases} u_j^{\pm} \qquad \forall j \in T.$$

(3) For each node i, compute the quantities:

$$\bar{u}_i^{\pm} = \begin{cases} \max \\ \min \end{cases} u_T^{\pm} \quad \forall T \in \Delta_i,$$

namely, the extreme values that the solution may assume at node i, i.e., $\bar{u}_i^- \leqslant u_i^{n+1} \leqslant \bar{u}_i^+$.

(4) For each node i, compute the quantities:

$$\Delta u_i^{\pm} = \begin{cases} \max \\ \min \end{cases} (0, u_i^{\mathrm{ho}} - \bar{u}_i^{\pm}), \quad \rightarrow \quad \Delta f_i^{\pm} = \Delta u_i^{\pm} \frac{|S_i|}{\Delta t}.$$

$\Delta u_i^{\pm}$ are different from zero only if the higher-order solution, u_i^{ho}, lies outside the monotonicity bounds, $\bar{u}_i^{\pm}$, and $\Delta f_i^{\pm}$ are the corresponding fluxes. In order to have monotone solutions, all $\Delta u_i^{\pm}(\Delta f_i^{\pm})$ must vanish. Update the solution as:

$$\tilde{u}_i = u_i^{\mathrm{ho}} - \Delta f_i^{\pm} \frac{\Delta t}{|S_i|}.$$

(5) For each node i, compute the quantities:

$$\Delta u_{i,\max}^{\pm} = \begin{cases} \max \\ \min \end{cases} (0, \bar{u}_i^{\pm} - \tilde{u}_i), \quad \rightarrow \quad \Delta f_{i,\max}^{\pm} = \Delta u_{i,\max}^{\pm} \frac{|S_i|}{\Delta t}.$$

$\Delta u_{i,\max}^{\pm}$ are different from zero if the solution, $\tilde{u}_i$, lies within the prescribed bounds, $\bar{u}_i^- < \tilde{u}_i < \bar{u}_i^+$; $\Delta f_{i,\max}^{\pm}$ are the associated flux variations over the median dual cell, which are the distances of the solution from the allowed monotonicity bounds.

(6) For each node i such that $\Delta f_i^+ > 0$ $(\Delta f_i^- < 0)$, evaluate

$$\mathscr{F}_{i,\max}^{\pm} = \sum_j \Delta f_{j,\max}^{\pm}, \quad j \in \Delta_i, \; j \neq i,$$

which represent the fluctuation contributions that the nodes surrounding node i may receive without violating the monotonicity constraints.

If $\mathscr{F}_{i,\max}^{+} \geqslant \Delta f_i^+ (\mathscr{F}_{i,\max}^{-} \leqslant \Delta f_i^-)$, then redistribute $\Delta f_i^{\pm}$ among the surrounding nodes, j, proportionally to $\Delta f_{j,\max}^{\pm}$:

$$\Delta f_{ij}^{\pm} = \Delta f_i^{\pm} \frac{\Delta f_{j,\max}^{\pm}}{\mathscr{F}_{i,\max}^{\pm}},$$

else,

$$\Delta f_{ij}^{\pm} = \Delta f_{j,\max}^{\pm}, \quad R_i^{\pm} = \Delta f_i^{\pm} - \mathscr{F}_{i,\max}^{\pm}.$$

Notice that $\Delta f_{i,\max}^{\pm}$ needs to be updated throughout every sweep as:

$$\Delta f_{j,\max}^{\pm} = \Delta f_{j,\max}^{\pm} - \Delta f_{ij}^{\pm}, \quad j \in \Delta_i, \; j \neq i.$$

Finally, update the solution as:

$$\tilde{u}_j = u_j^{\mathrm{ho}} + (\Delta f_{ij}^{+} + \Delta f_{ij}^{-}) \frac{\Delta t}{|S_i|}, \quad j \in \Delta_i, \; j \neq i,$$

where $\tilde{u} = u^{n+1}$, when the entire domain has been swept. For the rare situations in which the quantity $R_i^{\pm}$ is not equal to zero, it is distributed among the next row of neighbouring points according to the criterion explained at point 6, namely proportionally to $\Delta f_{j,\max}^{\pm}$.

The core of the proposed algorithm are steps 4 and 6: in step 4, for each dual cell, a flux difference associated to the fraction of the correction which violates monotonicity is determined, whereas, in step 6, such a

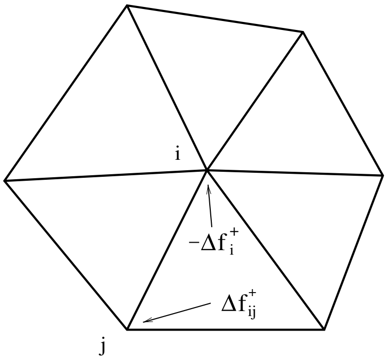

Fig. 4. Redistribution step.

flux difference is distributed among the vertices of the dual cell as shown in Fig. 4. It is noteworthy that the main merit of the proposed procedure is that the limiting strategy is imposed on residuals at each node, thus allowing to reduce the unsteady residual at will, down to machine accuracy.

Finally, concerning the choice of the limiting lower-order scheme, the N scheme has been employed in all computations performed in the present work, so that each limited scheme will be labelled by adding -N to the label of the corresponding linear scheme. It is noteworthy that the implicit N-scheme of [24], which is unconditionally stable and monotone, is used here in order to guarantee stable and monotone solutions for CFL numbers greater than those allowed by explicit schemes. Such a scheme evaluates the residual at the new time step while discretizing the pseudo-time derivative by a two-point difference and employing a lumped mass matrix $(m_{i,j} = \frac{1}{3}|T|I)$.

4. Extension to hyperbolic systems

4.1. Linear matrix FS schemes

The Euler equations are written in conservative form as:

$$\frac{\partial U}{\partial t} = -\frac{\partial F}{\partial x} - \frac{\partial G}{\partial y}, \tag{33}$$

where

$$U = \begin{pmatrix} \rho \\ \rho u \\ \rho v \\ \rho E \end{pmatrix}, \quad F = \begin{pmatrix} \rho u \\ p + \rho u^2 \\ \rho u v \\ \rho u H \end{pmatrix}, \quad G = \begin{pmatrix} \rho v \\ \rho u v \\ p + \rho v^2 \\ \rho v H \end{pmatrix}, \tag{34}$$

are the vectors of the conservative variables and of the fluxes in the x and y directions, respectively.

In order to apply the proposed FS scheme, Eq. (33) need to be rewritten in their quasi-linear form:

$$\frac{\partial U}{\partial t} = -\left(A\frac{\partial U}{\partial x} + B\frac{\partial U}{\partial y}\right), \tag{35}$$

where $A = \partial F/\partial U$ and $B = \partial G/\partial U$ are the Jacobian matrices. The computational domain is discretized by linear finite elements (triangles).

The conservative flux balance over each triangle T is defined as the fluctuation, Φ_T,

$$\Phi_T = -\int_T \left(A\frac{\partial U}{\partial x} + B\frac{\partial U}{\partial y} \right) \mathrm{d}S. \tag{36}$$

The discrete counterpart of Eq. (36) requires a conservative linearization in order to compute shocks correctly. By assuming the parameter vector $Z = \sqrt{\rho}(1, u, v, H)^{\tau}$ to vary linearly over each triangle, the discrete fluctuation can be evaluated analytically as:

$$\Phi_T = -\left(\bar{A}\overline{\frac{\partial U}{\partial x}} + \bar{B}\overline{\frac{\partial U}{\partial y}} \right) |T|, \tag{37}$$

the bar indicating suitable cell-averaged values [9]. The fluctuation Φ_T is then rewritten in terms of appropriate fluxes through the sides of each triangle (see [25,26], for details) as:

$$\Phi_T = -\sum_{j=1}^{3} \frac{l_j}{2} \bar{\boldsymbol{A}} \cdot \boldsymbol{n}_j U_j = -\sum_{j=1}^{3} K_j U_j, \tag{38}$$

where

$$K_j = \frac{1}{2} l_j \left(\bar{A} n_{x,j} + \bar{B} n_{y,j} \right). \tag{39}$$

Due to the hyperbolic nature of the system, K_j can be written as

$$K_j = (\bar{R}_K \bar{\Lambda}_K \bar{L}_K)_j = (\bar{R}_K \bar{\Lambda}_K^{+} \bar{L}_K)_j + (\bar{R}_K \bar{\Lambda}_K^{-} \bar{L}_K)_j = K_j^{+} + K_j^{-}. \tag{40}$$

In Eq. (40), $\bar{R}_{K,j}$ and $\bar{L}_{K,j}$ are the right and left eigenvector matrices of K_j, whereas $\bar{\Lambda}_{K,j}^{+}$ and $\bar{\Lambda}_{K,j}^{-}$ are the corresponding positive and negative eigenvalue matrices. In such a way, it is possible to provide linear matrix FS schemes for the Euler system, by extending the definition of the corresponding scalar ones, retaining the same properties. In fact, introducing the following vector:

$$U_{\mathrm{in}} = \left(\sum_{j=1}^{3} K_j^{-} \right)^{-1} \left(\sum_{j=1}^{3} K_j^{-} U_j \right), \tag{41}$$

the linear matrix N scheme [25,26] is obtained as:

$$\Phi_j^{\mathrm{N}} = -K_j^{+} \left[U_j - U_{\mathrm{in}} \right]. \tag{42}$$

The non-upwind matrix FS-LW scheme does not require any splitting and is simply given as:

$$\Phi_j^{\mathrm{LW}} = \left(\frac{1}{3} I + \frac{\Delta t}{2|T|} K_j \right) \Phi_T. \tag{43}$$

Finally, the matrix UCV scheme is given as:

$$\Phi_j^{\mathrm{UCV}} = \left[\frac{1}{3} I + \frac{2}{3} \left(\sum_{i=1}^{3} |K_i| \right)^{-1} K_j \right] \Phi_T, \tag{44}$$

where $|K_i| = (\bar{R}_K |\bar{\Lambda}_K| \bar{L}_K)_i$.

4.2. The FCT explicit scheme

The FS-FCT scheme for the Euler system is obtained, like for the scalar case, as follows.

(1) For each node j of each element T, compute Φ_j^{N}, Φ_j^{LW}, and

$$AC_j = \frac{\Delta t}{|S_j|}\left(\Phi_j^{\mathrm{LW}} - \Phi_j^{N}\right).$$

(2) For each node i of the domain, compute the lower-order solution as:

$$U_i^{\mathrm{lo}} = U_i^n + \frac{\Delta t}{|S_i|}\sum_T \Phi_{T,i}^{\mathrm{N}}.$$

(3) For each element, evaluate the scalar limiter σ_T as described in the previous section, replacing u with any scalar dependent variable.

(4) For each node i of the domain, compute the final solution at the new time level $n + 1$ as follows:

$$U_i^{n+1} = U_i^{\mathrm{lo}} + \sum_{T\in\Delta_i} \sigma_T AC_i^T.$$

It is noteworthy that different choices of the limiting scalar variable are possible. During this study, the density, the total internal energy per unit volume, and the magnitude of the solution vector have been used, leading to only minor differences in the solutions. In all calculations presented in the result section, the density has been used to evaluate the limiting factor σ_T.

4.3. Implicit scheme

The proposed implicit FS scheme is extended to the Euler equations, by generalizing the results of Eqs. (11)–(25) as follows:

$$\Phi_{T,i}^t = |T|\boldsymbol{\beta}_{T,j}\sum_{j=1}^{3}\Gamma_{i,j}\left(\frac{\partial U}{\partial t}\right)_j, \tag{45}$$

with

$$\Gamma_{i,i} = \frac{1}{3}\left(2I - \boldsymbol{\beta}_{T,i}\right), \qquad \Gamma_{i,j} = \frac{1}{3}\left(I - \boldsymbol{\beta}_{T,i}\right), \quad j \neq i, \tag{46}$$

where $\Phi_{T,i}^t$ is the unsteady contribution sent to node i, and $\boldsymbol{\beta}_{T,i}$ is the distribution matrix to node i. The limiting procedure of Section 3 is applied to each single equation, straightforwardly.

5. Results

5.1. Scalar advection equation

Firstly, the accuracy of the proposed schemes has been tested by computing the advection of the double sine wave function $u(x,y,t)$

$$u(x, y, 0) = \sin(2\pi x)\sin(2\pi y),$$

by the velocity $\boldsymbol{\lambda} = (1,2)^\tau$, in the square domain $[0,1]^2$, with periodic boundary conditions, up to time $t = 1$. The computational domain has been discretized by uniform Cartesian grids, each quad-cell being divided

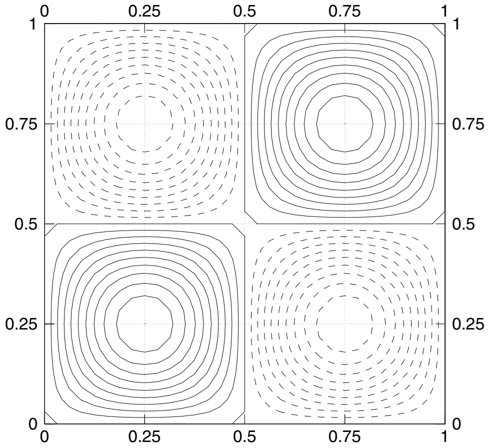

Fig. 5. Double sine wave function: exact solution, $u_{\max} = 1$, $u_{\min} = -1$, $\Delta u = 0.1$.

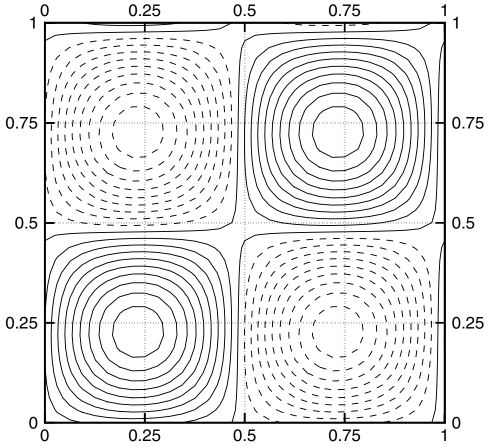

Fig. 6. Double sine wave function: FS-LW scheme, $u_{\max} = 0.9784$, $u_{\min} = -0.9784$, $\Delta u = 0.1$.

by the right-running diagonal. Fig. 5 provides the exact solution at $t = 1$ on the $\Delta x = \Delta y = 1/32$ grid, the dashed lines indicating negative values. Figs. 6–9 provide the corresponding numerical solutions obtained using the FS-LW, MM-C, MM-SU, and MM-CU schemes, respectively. It appears that the MM-C scheme is markedly more dissipative than the other ones which provide similar solutions. The solutions obtained by the MM-PG and FS-FCT schemes are also very similar and are not reported for the sake of brevity. On the other hand, a more thorough analysis has been performed by a mesh-refinement study, using six grids, starting from $\Delta x = \Delta y = 1/16$, $\Delta t = 0.02$ and halving both the space and time steps. The L_1 and L_∞ norms of the solution error for both linear and nonlinear schemes are plotted in Figs. 10 and 11, respectively. Such values are also provided in Tables 1 and 2 for easier comparison by other investigators. The mesh-refinement study shows that the MM-C scheme is indeed only first-order-accurate, as anticipated, whereas the others are second-order-accurate, the implicit schemes providing lower errors than the explicit ones. Furthermore, for the present test-case, the proposed MM-CU and MM-CU-N schemes provide slightly higher errors than those of the MM-SU and MM-SU-N schemes, respectively. The errors provided by the MM-PG method, employing the UCV scheme, are also reported in Tables 1 and 2, and are very close to the ones

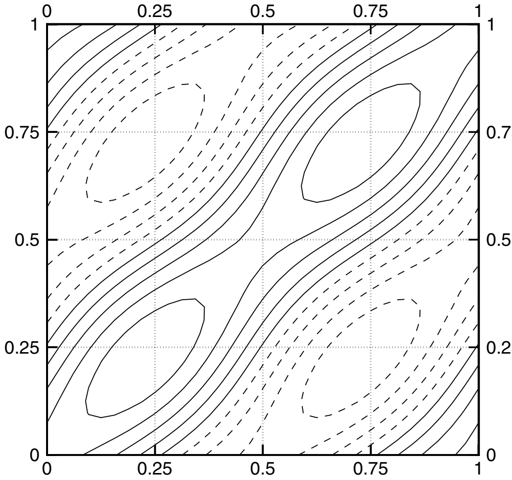

Fig. 7. Double sine wave function: MM-C scheme, $u_{\max} = 0.4874$, $u_{\min} = -0.4874$, $\Delta u = 0.1$.

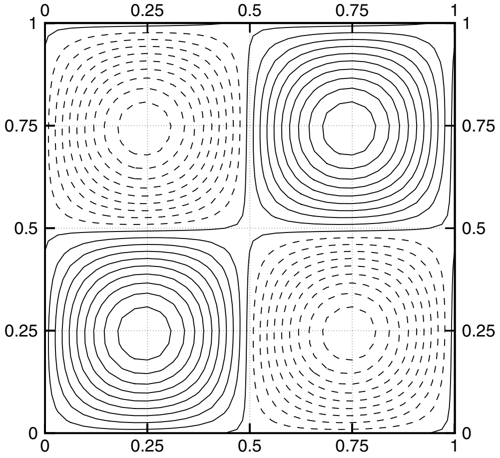

Fig. 8. Double sine wave function: MM-SU scheme, $u_{\max} = 0.9824$, $u_{\min} = -0.9824$, $\Delta u = 0.1$.

of the MM-CU scheme. For such a simple test case, the errors obtained using the LDA scheme in conjunction with the MM-PG method (not shown) are not significantly different. It is noteworthy that, due to the smoothness of the solution, the proposed limiting procedure does not affect second-order accuracy; on the other hand, using the FS-FCT scheme the convergence of the L_∞ norm deteriorates when refining the mesh.

Then, a second well documented test problem, namely, the circular advection of a smooth hump, $u(r,t)$ has been considered:

$$u(r,0) = \begin{cases} \cos^2(2\pi r) & \text{for } r \leqslant 0.25, \\ 0 & \text{for } r > 0.25, \end{cases} \tag{47}$$

in the square domain $[-1, 1]^2$, up to time $t = 1$, by the velocity $\boldsymbol{\lambda} = (-2\pi y, 2\pi x)^\tau$, where $r^2 = (x + 0.5)^2 + y^2$. The hump follows a circular path and returns to its initial position at $t = 1$. A mesh-refinement study has been performed using a set of six structured grids (mesh C) and a set of six unstructured grids (mesh U). The first set of computations has been performed starting from a grid with $\Delta x = \Delta y = 1/16$, $\Delta t = 0.01$ and

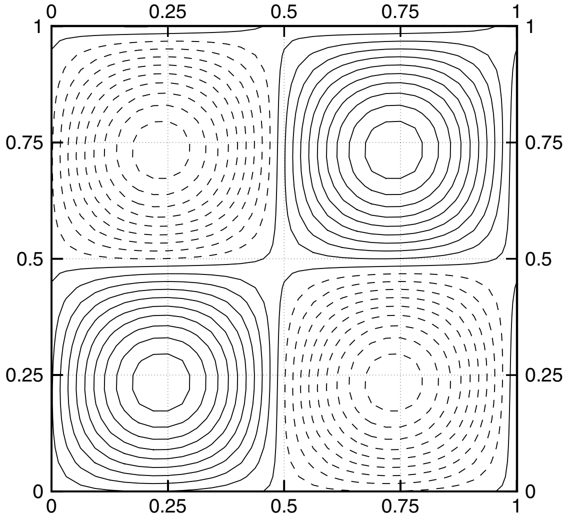

Fig. 9. Double sine wave function: MM-CU scheme, $u_{\max} = 0.9684$, $u_{\min} = -0.9684$, $\Delta u = 0.1$.

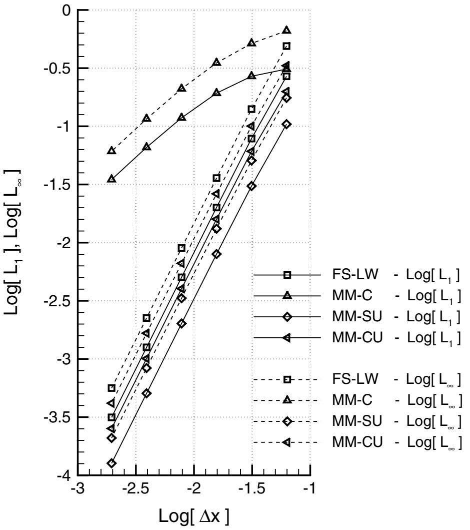

Fig. 10. Double sine advection problem: accuracy study for linear schemes.

halving both the space and time steps. The second set of computations has been performed starting from an unstructured grid with 280 points, 494 triangular cells, $\Delta t = 0.01$, and dividing each triangle into four sub-triangles introducing the mid-points of the edges as new vertices, while halving the time step. The L_1 and L_∞ norms of the solution error for the FS-LW, MM-C, MM-SU, MM-PG and MM-CU schemes are plotted in Figs. 12 and 13, respectively. The mesh-refinement study confirms that the MM-C scheme is only first-order-accurate, as anticipated, whereas the other schemes are second-order-accurate, the MM-PG and MM-CU ones providing lower errors. It is noteworthy that using the LDA scheme instead of the UCV one in conjunction with the MM-PG method, as originally proposed in [14], provides slightly higher errors. It is clearly seen that the differences between the results obtained using the two sets of structured and

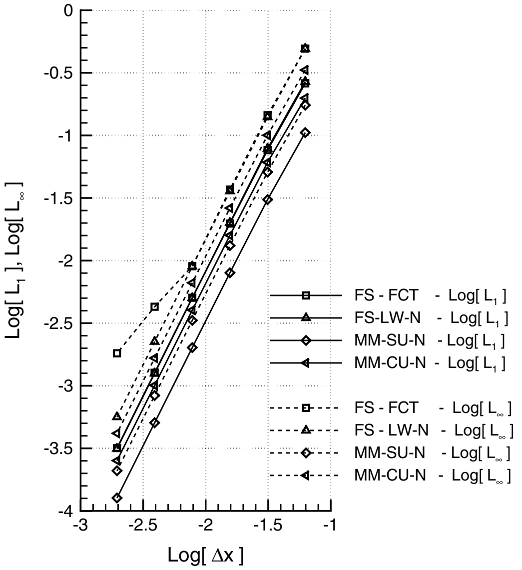

Fig. 11. Double sine advection problem: accuracy study for nonlinear schemes.

Table 1
Double sine advection problem: accuracy study, L_1 norm

	16 × 16	32 × 32	64 × 64	128 × 128	256 × 256	512 × 512
FS-LW	2.689E − 1	7.845E − 2	2.005E − 2	5.030E − 3	1.258E − 3	3.146E − 4
MM-C	3.105E − 1	2.693E − 1	1.926E − 1	1.182E − 1	6.592E − 2	3.487E − 2
MM-SU	1.043E − 1	3.063E − 2	7.975E − 3	2.017E − 3	5.065E − 4	1.269E − 4
MM-CU	1.988E − 1	6.095E − 2	1.591E − 2	4.021E − 3	1.009E − 3	2.524E − 4
MM-PG	2.157E − 1	6.692E − 2	1.749E − 2	4.421E − 3	1.109E − 3	2.773E − 4
FS-FCT	2.605E − 1	7.630E − 2	1.977E − 2	5.045E − 3	1.271E − 3	3.177E − 4
FS-LW-N	2.686E − 1	7.844E − 2	2.005E − 2	5.029E − 3	1.258E − 3	3.146E − 4
MM-SU-N	1.053E − 1	3.072E − 2	7.984E − 3	2.018E − 3	5.066E − 4	1.269E − 4
MM-CU-N	1.987E − 1	6.093E − 2	1.591E − 2	4.021E − 3	1.009E − 3	2.524E − 4

Table 2
Double sine advection problem: accuracy study, L_∞ norm

	16 × 16	32 × 32	64 × 64	128 × 128	256 × 256	512 × 512
FS-LW	4.891E − 1	1.405E − 1	3.586E − 2	8.992E − 3	2.249E − 3	5.624E − 4
MM-C	6.624E − 1	5.157E − 1	3.505E − 1	2.102E − 1	1.159E − 1	6.099E − 2
MM-SU	1.755E − 1	5.077E − 2	1.317E − 2	3.330E − 3	8.357E − 3	2.093E − 4
MM-CU	3.318E − 1	1.004E − 1	2.628E − 2	6.640E − 3	1.665E − 3	4.168E − 4
MM-PG	3.546E − 1	1.087E − 1	2.849E − 2	7.199E − 3	1.805E − 3	4.513E − 4
FS-FCT	4.931E − 1	1.449E − 1	3.692E − 2	9.017E − 3	4.279E − 3	1.817E − 3
FS-LW-N	4.935E − 1	1.402E − 1	3.587E − 2	8.993E − 3	2.249E − 3	5.624E − 4
MM-SU-N	1.744E − 1	5.093E − 2	1.317E − 2	3.330E − 3	8.357E − 3	2.093E − 4
MM-CU-N	3.329E − 1	1.004E − 1	2.628E − 2	6.640E − 3	1.665E − 3	4.168E − 4

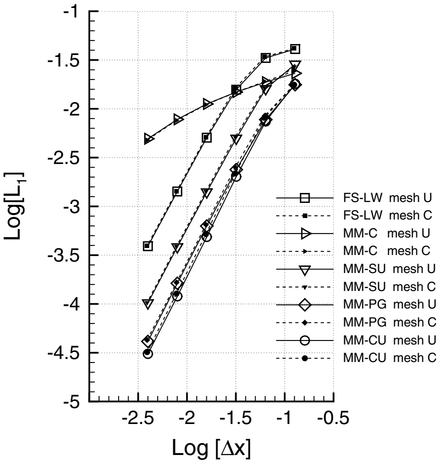

Fig. 12. Rotating hump: accuracy study for linear schemes, L_1 norm of the solution error.

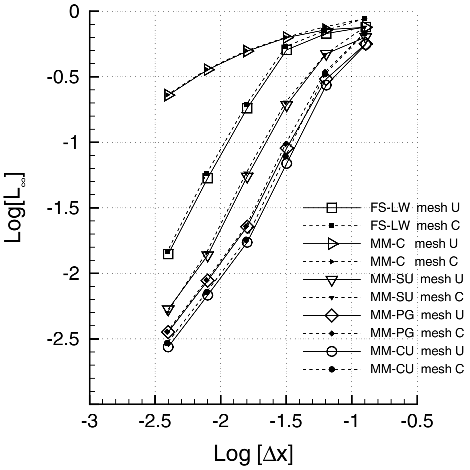

Fig. 13. Rotating hump: accuracy study for linear schemes, L_∞ norm of the solution error.

unstructured grids are quite negligible, confirming that fluctuation splitting schemes, due to their multidimensional nature, are very well suited to unstructured grids. It is noteworthy that using the MM-CU scheme with the 128 × 128-mesh C (31,616 elements for mesh U) one obtains about the same errors as the explicit FS-LW scheme on the 512 × 512-mesh C (505,856 elements for mesh U). Considering that, for such a test-case, the number of inner iterations needed to reduce the L_∞ norm of the unsteady residual to 10^{-7} is about 10, the cost of the implicit computation is about 1/6.4 than that of the FS-LW scheme, for a comparable accuracy. Needless to say, such an occurrence is problem dependent and by no means one can state that the MM-CU scheme is six times more efficient than the FS-LW one, in particular for the Euler system, see Section 5.2. The same test case has been solved employing two grids: a uniform Cartesian grid with 89 × 89 quad-cells, divided into triangles by means of the right-running diagonals; and an unstructured grid with 8061 nodes and 15,800 triangular cells, shown in Fig. 14. Such a grid contains about the same

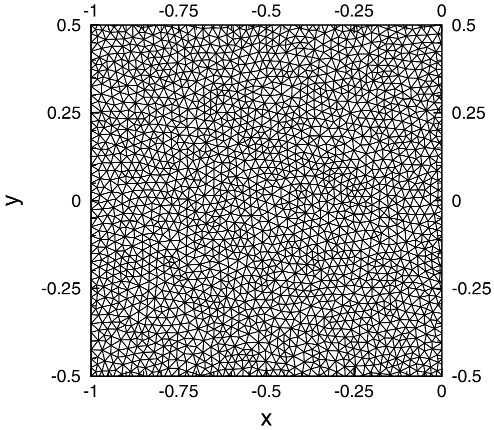

Fig. 14. Rotating hump: local view of the unstructured grid (mesh U).

number of points (8079) and of triangular cells (15,836) employed in [19] for solving the same problem, so that a direct comparison between the two solutions is possible. For both grids, the time step has been evaluated with respect to the unstructured mesh according to [19] as:

$$\Delta t = \frac{2}{3} CFL \min_i \frac{|T|}{k_i^+},$$

with $CFL = 0.9$, and is equal to 1.81×10^{-3}. Figs. 16–25 provide the level lines of the solutions at $t = 1$ obtained using the FS-LW, MM-C, MM-SU, MM-PG and MM-CU schemes, respectively; Fig. 15 shows the exact solution, for comparison. Such figures confirm that the differences between the solutions obtained on mesh U and mesh C are quite negligible. It appears that: the FS-LW scheme provides a significant phase error; the MM-C scheme, due to its first-order accuracy, is clearly too dissipative; and the MM-SU, MM-PG and MM-CU schemes provide very similar level lines. Moreover, the solutions of the MM-CU/UCV (MM-PG/UCV) and MM-CU/LDA (MM-PG/LDA) schemes – not shown – are almost indistinguishable. Figs. 26–29 provide the level lines obtained employing the FS-LW-N and MM-CU-N schemes. The solutions obtained on mesh U and mesh C are again almost indistinguishable. Both schemes provide monotone

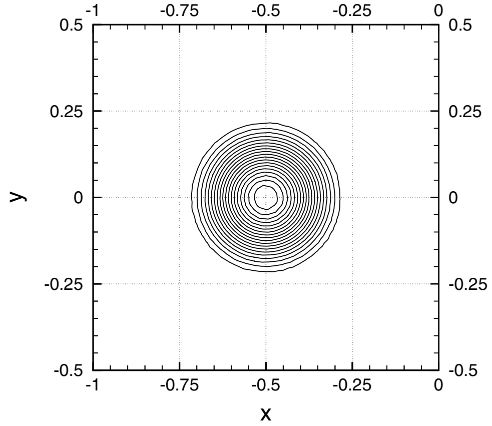

Fig. 15. Rotating hump: exact solution at $t = 1$ ($\Delta u = 0.05$).

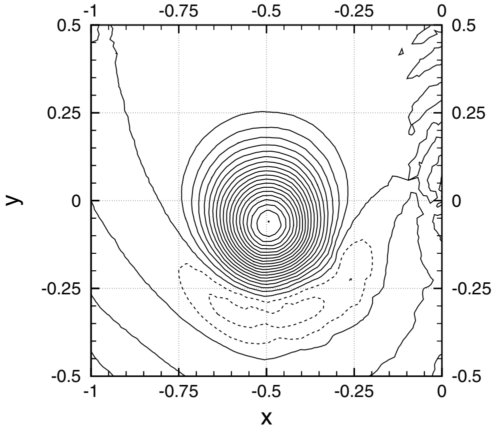

Fig. 16. Rotating hump: numerical solution at $t = 1$ using the FS-LW scheme and the unstructured grid ($\Delta u = 0.05$).

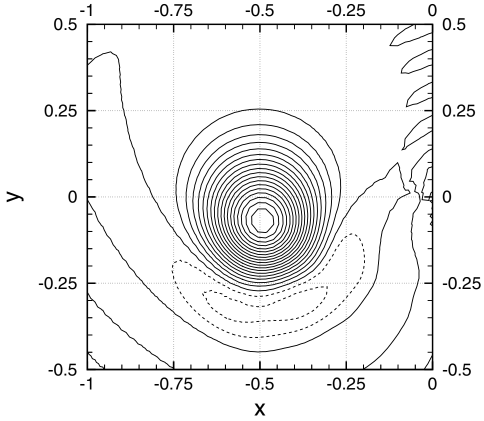

Fig. 17. Rotating hump: numerical solution at $t = 1$ using the FS-LW scheme and the structured grid ($\Delta u = 0.05$).

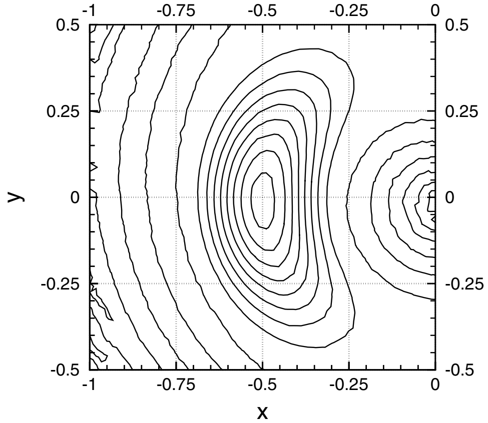

Fig. 18. Rotating hump: numerical solution at $t = 1$ using the MM-C scheme and the unstructured grid ($\Delta u = 0.05$).

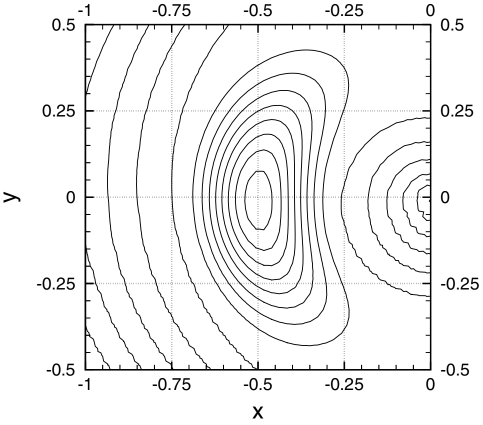

Fig. 19. Rotating hump: numerical solution at $t = 1$ using the MM-C scheme and the structured grid ($\Delta u = 0.05$).

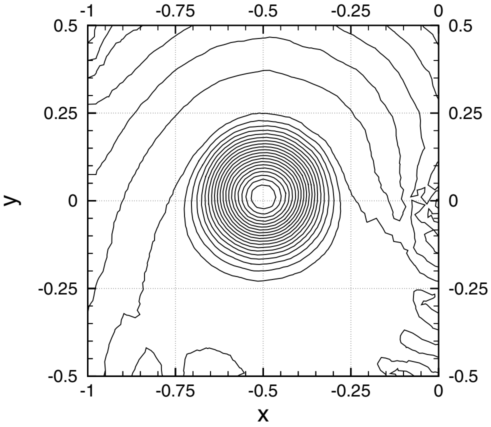

Fig. 20. Rotating hump: numerical solution at $t = 1$ using the MM-SU scheme and the unstructured grid ($\Delta u = 0.05$).

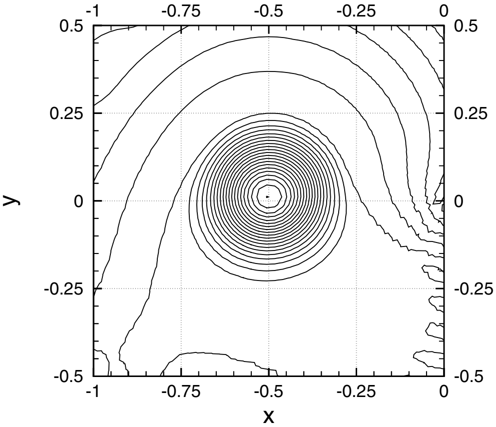

Fig. 21. Rotating hump: numerical solution at $t = 1$ using the MM-SU scheme and the structured grid ($\Delta u = 0.05$).

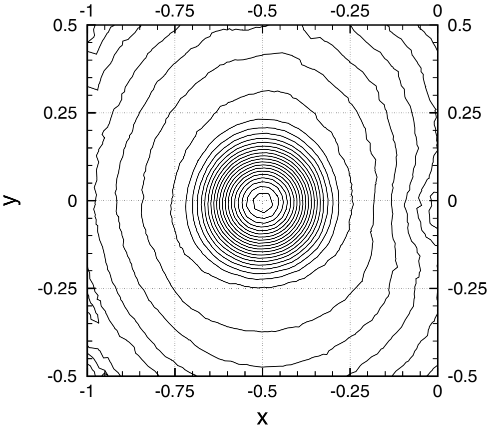

Fig. 22. Rotating hump: numerical solution at $t = 1$ using the MM-PG scheme and the unstructured grid ($\Delta u = 0.05$).

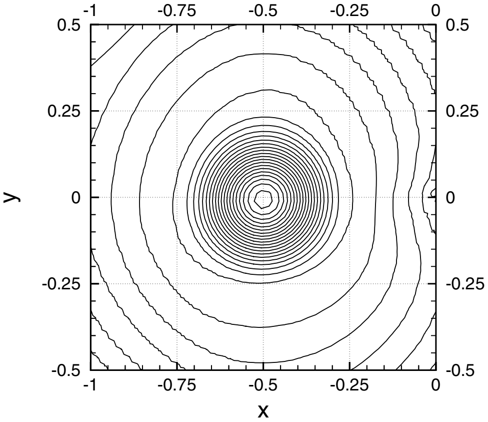

Fig. 23. Rotating hump: numerical solution at $t = 1$ using the MM-PG scheme and the structured grid ($\Delta u = 0.05$).

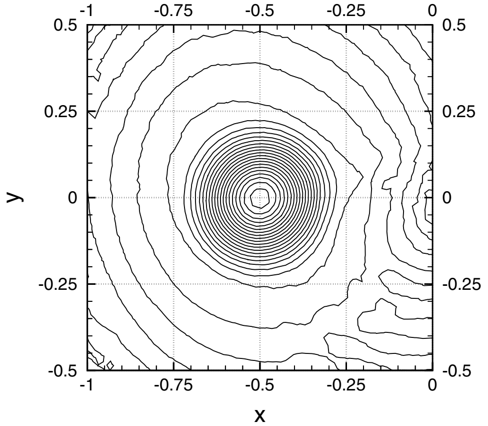

Fig. 24. Rotating hump: numerical solution at $t = 1$ using the MM-CU scheme and the unstructured grid ($\Delta u = 0.05$).

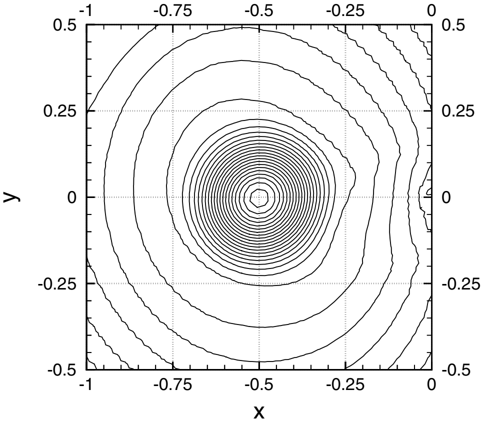

Fig. 25. Rotating hump: numerical solution at $t = 1$ using the MM-CU scheme and the structured grid ($\Delta u = 0.05$).

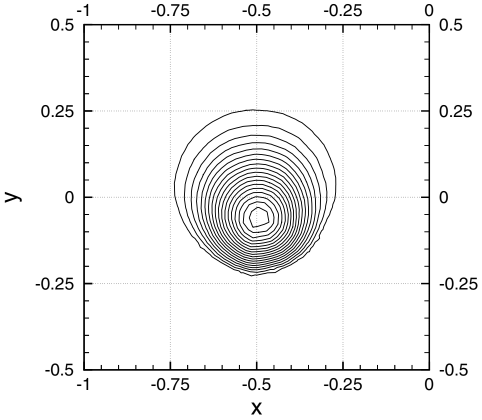

Fig. 26. Rotating hump: numerical solution at $t = 1$ using the FS-LW-N scheme and the unstructured grid ($\Delta u = 0.05$).

solutions, the MM-CU-N being clearly more accurate. Fig. 30 provides the vertical cuts of the solutions through the exact centre of the hump, $(-0.5,0)$, at $t = 1$, obtained on mesh U. The FS-LW solution shows large oscillations and errors, whereas the MM-CU scheme provides markedly lower amplitude and phase errors and very small oscillations. Moreover, the limiting procedure is seen to be effective in hampering local extrema, the solutions obtained with the FS-LW-N and MM-CU-N schemes being monotone. However, the limiting procedure reduces the maximum value of the numerical solution as also shown in Table 3. It is noteworthy that, for such a smooth solution, the present nonlinear procedure introduces less dissipation with respect to the nonlinear approach proposed in [19], as demonstrated by the results obtained using the N-modified scheme, which were provided in [19] and are reported in the table.

Finally, the circular advection of a cylinder, $u(r,t)$ in the square domain $[-1,1]^2$ has been computed to verify the monotonicity of the proposed schemes,

$$u(r,0) = \begin{cases} 1 & \text{for } r \leqslant 0.25, \\ 0 & \text{for } r > 0.25, \end{cases} \tag{48}$$

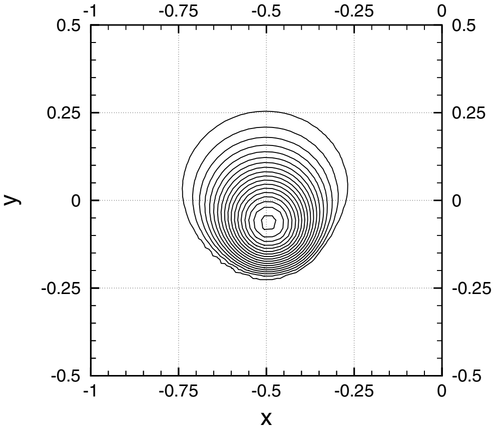

Fig. 27. Rotating hump: numerical solution at $t = 1$ using the FS-LW-N scheme and the structured grid ($\Delta u = 0.05$).

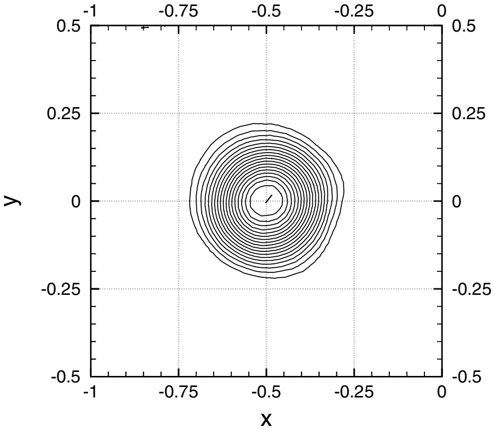

Fig. 28. Rotating hump: numerical solution at $t = 1$ using the FS-CU-N scheme and the unstructured grid ($\Delta u = 0.05$).

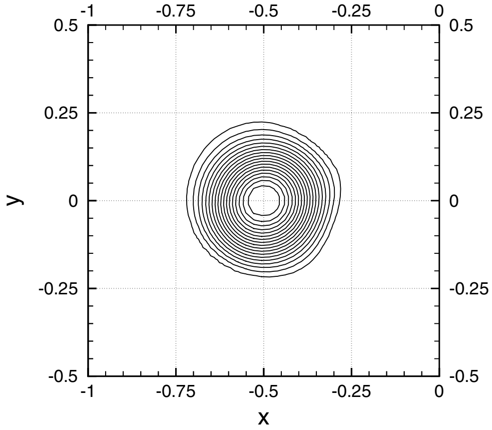

Fig. 29. Rotating hump: numerical solution at $t = 1$ using the FS-CU-N scheme and the structured grid ($\Delta u = 0.05$).

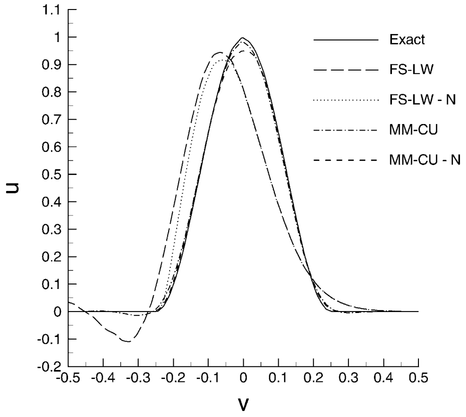

Fig. 30. Rotating hump: vertical cut at $t = 1$ using the unstructured grid.

Table 3
Rotating hump: maximum and minimum value of the solution at $t = 1$

Scheme	Min	Max
FS-LW	−0.1235	0.9511
MM-C	−0.0035	0.4253
MM-SU	−0.0488	0.9994
MM-PG	−0.0298	0.9824
MM-CU	−0.0237	0.9851
FS-LW-N	0	0.9215
MM-CU-N	0	0.9501
N-modified [19]	0	0.802

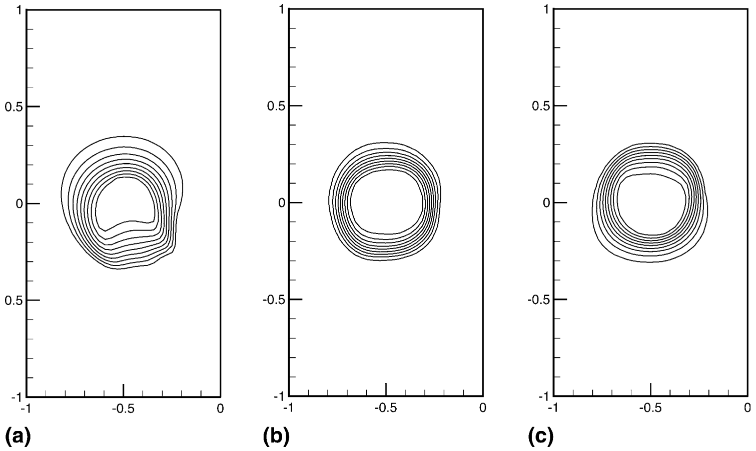

Fig. 31. Rotating cylinder: numerical solution at $t = 1$ using (a) the FS-LW-N scheme, (b) MM-CU-N scheme, (c) MM-SU-N scheme ($\Delta u = 0.1$).

where again $r^2 = (x + 0.5)^2 + y^2$ and $\boldsymbol{\lambda} = (-2\pi y, 2\pi x)^{\tau}$. A uniform Cartesian grid has been employed with 64×64 quad-cells, divided into triangles by means of the right-running diagonals. Fig. 31 provides the level lines obtained at $t = 1$ ($\Delta t = 0.0025$) using the FS-LW-N, MM-CU-N and MM-SU-N

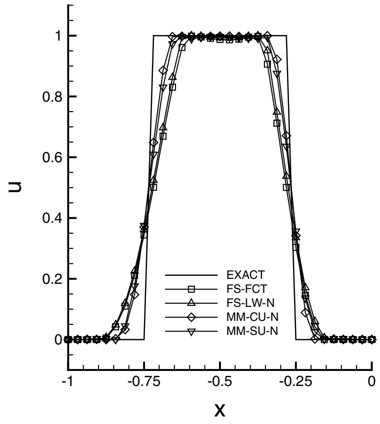

Fig. 32. Rotating cylinder: horizontal cut at $t = 1$.

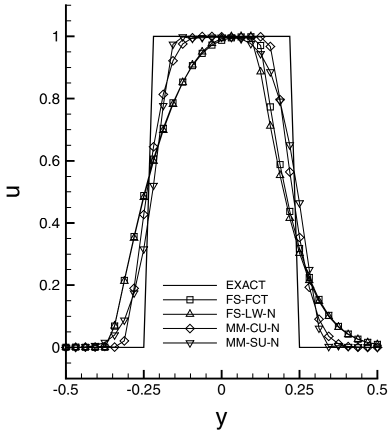

Fig. 33. Rotating cylinder: vertical cut at $t = 1$.

schemes, respectively. The level lines obtained using the FS-FCT scheme (not reported) coincide within plotting accuracy with those of the FS-LW-N one. Figs. 32 and 33 provide the corresponding horizontal and vertical solution cuts through the exact centre of the cylinder (−0.5,0). The exact solution is also provided, for completeness. All schemes provide monotone solutions, the implicit ones showing smaller dissipative and dispersive errors. It is noteworthy that the proposed MM-CU-N scheme enjoys the lowest dispersive error. In order to verify the monotonicity of such schemes even when employing larger time steps than that allowed by the explicit scheme, the previous test case has been recomputed employing the following time steps: $\Delta t = 0.005$, $\Delta t = 0.01$, and $\Delta t = 0.02$, corresponding to CFL numbers equal to 1.4, 2.8, and 5.6, respectively. Figs. 34 and 35 provide the horizontal and vertical cuts of the solutions through the exact centre; the results of Figs. 32 and 33 and the exact profiles are also given for comparison. The figures clearly demonstrate that the solutions remain monotone for increasing values of the time step, even when the (time) accuracy deteriorates significantly.

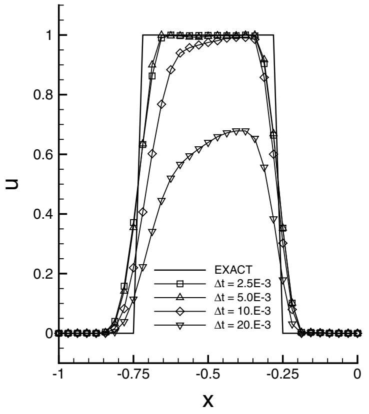

Fig. 34. Rotating cylinder: horizontal cut at $t = 1$.

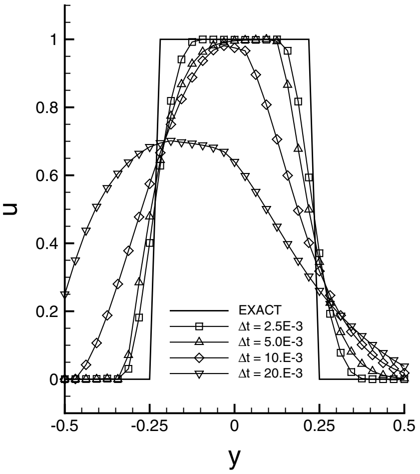

Fig. 35. Rotating cylinder: vertical cut at $t = 1$.

5.2. Euler equations

The accuracy of the proposed second-order schemes has been verified by computing the advection of a two-dimensional vortex superposed to a uniform flow with $(\rho, u, v, p) = (1, \sqrt{\gamma}, 0, 1)$, with $\gamma = 1.4$. The vortex, at $t = 0$, is given in polar coordinates (r,θ) as:

$$\begin{aligned} u^* &= \epsilon r \mathrm{e}^{\alpha(1-\tau^2)} \sin\theta, \\ v^* &= -\epsilon r \mathrm{e}^{\alpha(1-\tau^2)} \cos\theta, \\ T^* &= -\frac{(\gamma-1)\epsilon^2}{4\alpha} \mathrm{e}^{2\alpha(1-\tau^2)}, \end{aligned} \tag{49}$$

where $\tau = r/0.05$, $\epsilon = 0.3$, $\alpha = 0.204$, and θ is the counter-clockwise angle measured with respect to the horizontal direction. The two-dimensional computations are performed on the $[0,2] \times [0,1]$ domain up to $t = 0.2$, on a sequence of five grids, starting from $\Delta x = \Delta y = 1/20$ and $\Delta t = 0.0125$, and halving both the

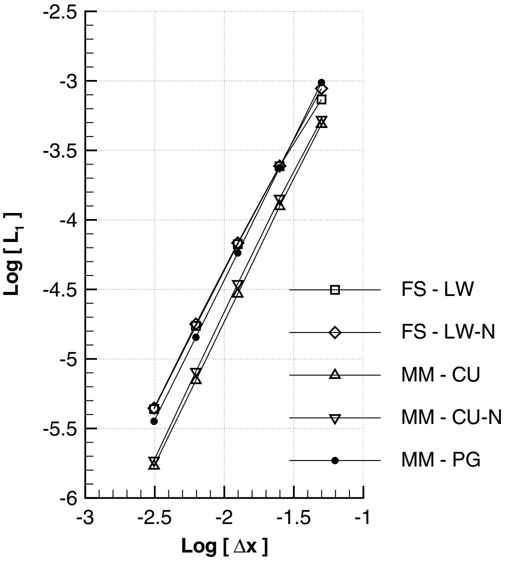

Fig. 36. Euler equations: accuracy study.

space and time steps. In Fig. 36, the L_1 norm of the density errors, obtained with the FS-LW, FS-LW-N, MM-CU, and MM-CU-N schemes, are provided. All schemes are second-order accurate, the implicit ones providing markedly lower errors. It is noteworthy that, the solution being smooth, the limiting procedure does not reduce the formal order of accuracy of the schemes. For comparison, results have also been obtained using the consistent mass matrix of Eq. (32) and the distribution coefficients of the LDA scheme [4], as proposed in [14]. The L_1 norm of the density error is shown in Fig. 36 (see the curve labelled MM-PG). The scheme is second-order accurate, as anticipated, but the errors appear greater that the ones provided by the MM-CU scheme and comparable to those of the explicit scheme.

The previous test case has been then recomputed reducing the uniform flow speed by a factor $10\sqrt{\gamma}$, considering $(\rho,u,v,p) = (1,0.1,0,1)$. Therefore, two time scales become relevant for such a problem, associated with the acoustic and advection speeds, respectively. Thanks to the great difference between such speeds, a slow transient results, which is suitable for comparing the performance of implicit versus explicit schemes. All computations have been performed using a grid with $\Delta x = \Delta y = 1/80$ for $0 \leqslant t \leqslant 5$. In order to test the stability and accuracy limits of the implicit MM-CU scheme, five values of $CFL_{\max}$ have been used, by successively doubling the one corresponding to the stability limit of the explicit scheme. All results are presented in Table 4 which provides the L_1 and L_∞ norms of the density error. It appears that the accuracy of the implicit scheme is clearly superior to that of the explicit one; more importantly, the error of the implicit scheme remains just about constant for values of the time step up to eight times larger than that allowed by

Table 4
Slow transient problem

	FS-LW	MM-CU				
Δt	6.25E − 3	6.25E − 3	1.25E − 2	2.5E − 2	5.E − 2	10.E − 2
$CFL_{\max}$	0.8	0.8	1.6	3.2	6.5	13
L_1	1.291E − 4	4.229E − 5	4.346E − 5	4.149E − 5	5.147E − 5	1.256E − 4
L_∞	8.577E − 3	4.773E − 3	4.830E − 3	4.915E − 3	5.303E − 3	9.915E − 3

the explicit scheme. Two considerations about the computational cost of the proposed implicit scheme are in order: each inner iteration of the implicit scheme, using an explicit Euler smoother, costs about three times one integration step of the cheapest explicit scheme, namely, the FS-LW one. The main additional cost (per iteration) is due to the need of computing the inverses of the matrices K_j for each element when using the UCV scheme (see Eq. (44)). Indicating with n the number of inner iterations needed to reduce the unsteady residual to a suitable value, the overall computational cost of a simulation using the implicit method, C_{imp}, with respect to the FS-LW scheme, C_{exp}, is given as:

$$C_{\mathrm{imp}} = \frac{3n\Delta t_{\mathrm{exp}}}{\Delta t_{\mathrm{imp}}} C_{\mathrm{exp}}.$$

In the case of Table 4, for $CFL_{\max} = 13$ one has about the same L_1 error norm provided by the FS-LW scheme; for such a computation $n = 60$ is needed to reduce the maximum L_∞ norm to 10^{-7}, therefore $C_{\mathrm{imp}} = 11.25C_{\mathrm{exp}}$. This is a rather discouraging result. However, the proposed method although not competitive, as far as its efficiency is concerned, for solving inviscid flows, may well turn out to become competitive for viscous flow computations, where stability is a much more relevant issue.

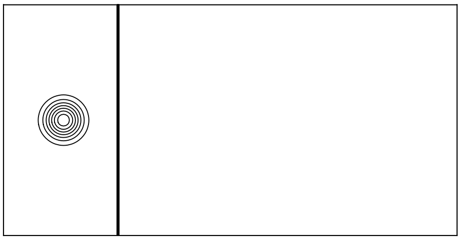

Fig. 37. Vortex–shock interaction: pressure contours at $t = 0$ ($\Delta p = 0.02$).

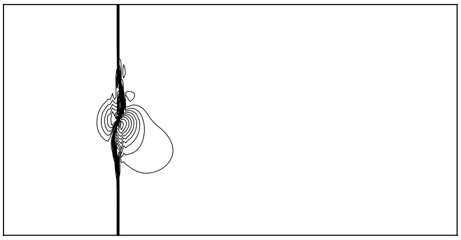

Fig. 38. Vortex–shock interaction: pressure contours at $t = 0.2$ using the FS-LW-N scheme ($\Delta p = 0.02$).

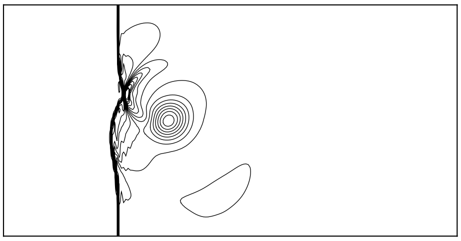

Fig. 39. Vortex–shock interaction: pressure contours at $t = 0.4$ using the FS-LW-N scheme ($\Delta p = 0.02$).

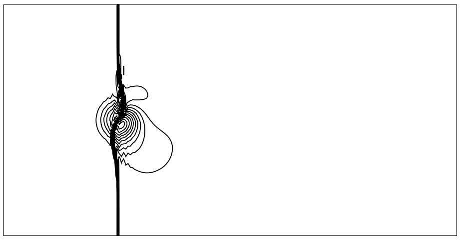

Fig. 40. Vortex–shock interaction: pressure contours at $t = 0.2$ using the MM-CU-N scheme ($\Delta p = 0.02$).

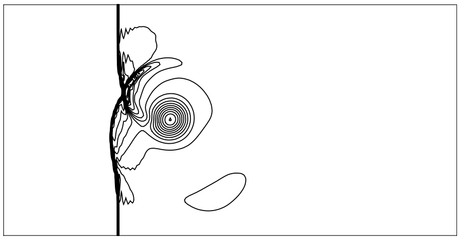

Fig. 41. Vortex–shock interaction: pressure contours at $t = 0.4$ using the MM-CU-N scheme ($\Delta p = 0.02$).

In order to test the proposed schemes versus a non-smooth problem, the advection of the vortex of Eq. (49) by a uniform supersonic flow

$$(\rho, u, v, p) = (1, 1.1\sqrt{\gamma}, 0, 1) \quad (M = 1.1),$$

impinging a steady vertical shock [19,27] has been computed in the $[0,2] \times [0,1]$ domain using 200×100 quad-cells and $\Delta t = 0.0025$. The pressure contours at the initial time are shown in Fig. 37. Figs. 38 and 39 provide the pressure contours at times $t = 0.2$ and $t = 0.4$, respectively, obtained using the FS-LW-N scheme; whereas Figs. 40 and 41 show the corresponding solutions obtained using the MM-CU-N scheme.

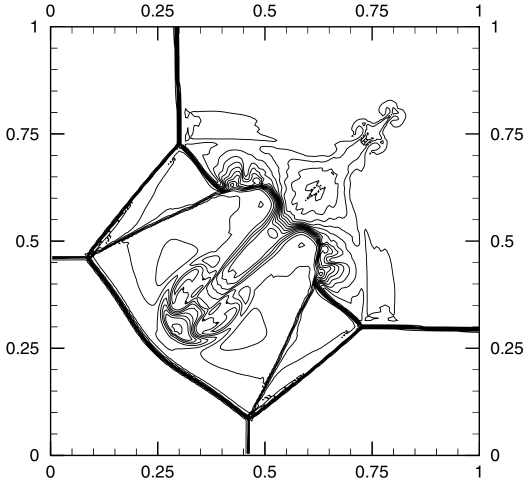

Fig. 42. Two-dimensional Riemann problem: density contours using the FS-FCT scheme ($\rho_{\min} = 0.138$, $\rho_{\max} = 1.778$, $\Delta\rho = 0.08$).

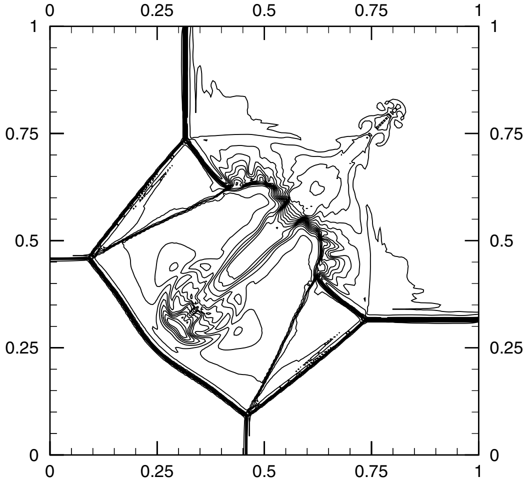

Fig. 43. Two-dimensional Riemann problem: density contours using the FS-LW-N scheme ($\rho_{\min} = 0.135$, $\rho_{\max} = 1.767$, $\Delta\rho = 0.08$).

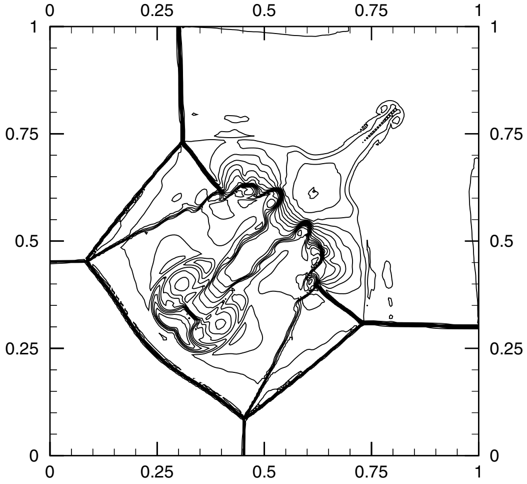

Fig. 44. Two-dimensional Riemann problem: density contours using the MM-CU-N scheme ($\rho_{\min} = 0.135$, $\rho_{\max} = 1.761$, $\Delta\rho = 0.08$).

Due to its lower dissipative error, the implicit scheme is able to provide a sharper shock and a well preserved vortex after the interaction ($t = 0.4$).

Finally, a very severe test-case has been considered, namely, the two-dimensional Riemann problem studied in [28]. The initial solution consists of four constant values in four quadrants chosen so that each pair of data gives a single shock wave, the interaction at the corner producing a complex structure, see [28] for details. The problem has been solved in the square domain $[0,1]^2$ on a grid with 200×200 quad-cells, with $\Delta t = 0.0016$, up to the final time $t = 0.8$. Figs. 42–44 provide the density contours obtained using the FS-FCT, FS-LW-N, and MM-CU-N schemes, respectively. All schemes provide sharp shocks and contact lines, but it appears that only the novel implicit scheme captures the Kelvin–Helmholtz instability of the slip lines already on this rather coarse grid, thanks to its low dissipative error. Notice that the

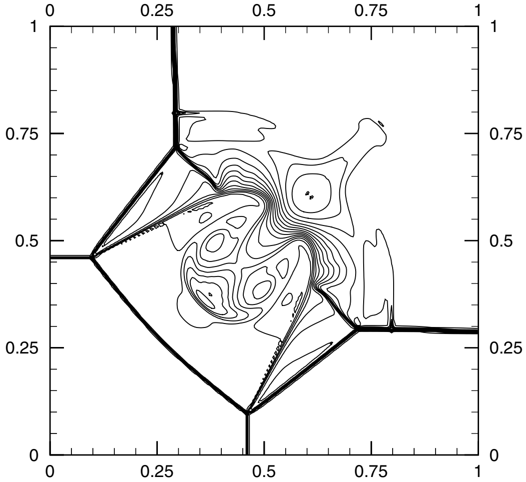

Fig. 45. Two-dimensional Riemann problem: density contours using the FV scheme of [28] without transverse propagation ($\rho_{\min} = 0.138$, $\rho_{\max} = 1.76$, $\Delta\rho = 0.08$).

MM-SU-N scheme fails for the present very difficult problem. Finally, Fig. 45 provides the solution obtained using the second-order-accurate finite-volume method of Le Veque [28] without transverse propagation, which represents a state-of-the-art scheme based on a direction-by-direction extension of one-dimensional models. The comparison demonstrates the remarkable improvement achieved employing genuinely multidimensional schemes, as also shown by Le Veque, who applies transverse propagation as a multidimensional correction, see figure 6 in [28].

6. Conclusions

A novel implicit methodology has been proposed, which extends to unsteady problems fluctuation splitting schemes previously designed for steady equations. The formulation is based on the definition of a general consistent mass matrix which guarantees second-order accuracy in space and time. Furthermore, a very effective new limiting procedure has been developed which is combined with the above methodology to achieve monotone solutions while locally introducing a very small dissipation. The method has been designed for the scalar advection equation and then extended to the Euler system. It has been applied with success to both scalar advection problems and very challenging compressible flow with shocks. Mesh refinement studies demonstrate that the proposed schemes achieve second-order accuracy in space and time for both the scalar advection equation and the Euler system. With respect to state-of-the-art methods for multidimensional unsteady advection problems, the proposed approach is characterized by a satisfactory robustness, which allowed to reduce the unsteady residual to machine zero in all performed computations, and very low dissipation especially in the nonlinear scheme. The drawback of the proposed approach lies in its computational cost. Future work will be devoted to the extension of the method to viscous flow computations where its merits in terms of stability may well render it competitive with current state-of-the-art methods.

Acknowledgements

The research has been supported by MIUR, grants Cofinlab2000 and Cofin2001.

References

[1] P.L. Roe, Characteristic-based schemes for the Euler equations, Ann. Rev. Fluid Mech. 18 (1986) 337–365.

[2] E. Godlewski, P. Raviart, Hyperbolic systems of conservation laws, Applied Mathematical Sciences, Springer, Berlin, 1995.

[3] B. Cockburn, C.-W. Shu, The local discontinuous Galerkin method for time-dependent convection–diffusion systems, SIAM J. Numer. Anal. 35 (6) (1998) 2440–2463.

[4] R. Struijs, H. Deconinck, P.L. Roe, Fluctuation splitting schemes for the 2D Euler equations, VKI LS 1991-01, Computational Fluid Dynamics, von Karman Institute, Belgium, 1991.

[5] E. van der Weide, H. Deconinck, E. Issmann, G. Degrez, Fluctuation splitting schemes for multidimensional convection problems: an alternative to finite volume and finite element methods, Comput. Mech. 23 (2) (1999) 199–208.

[6] P.L. Roe, Fluctuations and signals – a framework for numerical evolution problems, in: Numerical Methods for Fluid Dynamics, Proceedings Conference, Reading, 1982, pp. 219–257.

[7] R. Struijs, H. Deconinck, P. De Palma, P.L. Roe, K.G. Powell, Progress on multidimensional upwind Euler solvers for unstructured grids, AIAA Paper 91-1550, 1991.

[8] P.L. Roe, D. Sidilkover, Optimum positive linear schemes for advection in two and three dimensions, SIAM J. Numer. Anal. 29 (6) (1992) 1542–1588.

[9] H. Deconinck, P.L. Roe, R. Struijs, A multidimensional generalization of Roe's flux difference splitter for the Euler equations, Comput. Fluids 22 (1993) 215–222.

[10] H. Deconinck, R. Struijs, H. Paillère, L.A. Catalano, P. De Palma, M. Napolitano, G. Pascazio, Development of cell-vertex multidimensional upwind solvers for the compressible flow equations, CWI Quart. 6 (1) (1993) 1–28.

[11] L.A. Catalano, P. De Palma, G. Pascazio, M. Napolitano, Cell-vertex adaptive Euler method for cascade flows, AIAA J. 33 (12) (1995) 2299–2304.

[12] E. van der Weide, H. Deconinck, Positive matrix distribution schemes for hyperbolic systems, in: Computational Fluid Dynamics '96, 1996, pp. 747–753.

[13] A. Bonfiglioli, P. De Palma, G. Pascazio, M. Napolitano, An implicit fluctuation splitting scheme for turbomachinery flows, ASME J. Turbomach, in press (2005).

[14] J. März, G. Degrez, Improving time accuracy for residual distribution schemes, von Karman Institute Project Report 1996-17, 1996.

[15] A. Ferrante, H. Deconinck, Solution of the unsteady Euler equations using residual distribution and flux corrected transport, von Karman Institute Project Report 1997-08, 1997.

[16] M.E. Hubbard, P.L. Roe, Compact high resolution algorithms for time dependent advection problems on unstructured grids, Int. J. Numer. Methods Fluids 33 (2000) 711–736.

[17] Á. Csík, M. Ricchiuto, H. Deconinck, S. Poedts, Space–time residual distribution schemes for hyperbolic conservation laws, AIAA Paper 2001-2617, 2001.

[18] D. Caraeni, L. Fuch, Compact third-order multidimensional upwind scheme for Navier–Stokes simulations, Theoret. Comput. Fluid Dynamics 15 (2002) 373–401.

[19] R. Abgrall, M. Mezine, Construction of second order accurate monotone and stable residual distribution schemes for unsteady flow problems, J. Comput. Phys. 188 (2003) 16–55.

[20] R. Lohner, K. Morgan, M. Vahadati, J.P. Boris, D.L. Book, FEM-FCT: combining unstructured grids with high resolution, Commun. Appl. Numer. Methods 4 (1988) 717–729.

[21] P. De Palma, G. Pascazio, M. Napolitano, A second-order-accurate fluctuation splitting scheme for unsteady hyperbolic problems, Notes on Numerical Fluid Mechanics, vol. 78, Springer, New York, 2001, pp. 103–116.

[22] H. Paillère, Multidimensional upwind residual distribution schemes for the Euler and Navier–Stokes equations on unstructured grids, Ph.D Thesis, Université Libre de Bruxelles, Belgium, 1995.

[23] A. Jameson, Time dependent calculations using multigrid with applications to unsteady flows past airfoils and wings, AIAA Paper 91-1596, 1991.

[24] M. Mezine, M. Ricchiuto, R. Abgrall, H. Deconinck, Monotone and stable residual distribution schemes on prismatic space–time elements for unsteady conservation laws, von Karman Institute Lecture Series 2003-05, 2003.

[25] E. van der Weide, H. Deconinck, Positive matrix distribution schemes for hyperbolic systems, with applications to the Euler equations, Computational Fluid Dynamics '96, Wiley, New York, 1996, pp. 747–753.

[26] P. De Palma, G. Pascazio, M. Napolitano, A hybrid fluctuation splitting scheme for two-dimensional compressible steady flows, in: M.M. Hafez, J.J. Chattot (Eds.), Innovative Methods for Numerical Solution of Partial Differential Equations, World Scientific, New Jersey, 2002, pp. 305–333.

[27] K.R. Meadows, A. Kumar, M.Y. Hussaini, A computational study of the interaction between a vortex and a shock wave, AIAA Paper 89-1043, 1989.

[28] R.J. Le Veque, Wave propagation algorithms for multidimensional hyperbolic systems, J. Comput. Phys. 131 (1997) 327–353.